buildings

MDPI

Article

Experimental Study on Hysteretic Performance of Steel Moment Connection with Buckling-Restrained Dog-Bone Beam Sections

Shiqiang Feng [1,*], Yong Yang [1,2], Ning Hao [1], Xin Chen [1] and Jiancheng Zhou [1]

[1] School of Civil Engineering, Xi'an University of Architecture and Technology, Xi'an 710055, China
[2] Key Lab of Structural Engineering and Earthquake Resistance of the Ministry of Education, Xi'an University of Architecture and Technology, Xi'an 710055, China
* Correspondence: fengshiqiang@xauat.edu.cn

Abstract: Steel beam–column connections with dog-bone beam sections have gained significant attention and have been extensively applied. This is attributed to their ability to effectively centralize and integrate plastic hinges, thereby diverting potential damage away from the beam ends during earthquake events. In order to achieve the enhancement of the ductility and energy dissipation of connections by inhibiting local buckling during an earthquake event, a novel steel moment connection with buckling-restrained dog-bone beam sections was proposed in this paper. There were three types of proposed connections according to the different arrangements of restrained steel plates, including arranging the restrained plates only on the flanges, only on the web, and on both the flanges and webs of the dog-bone beam sections. In this study, three specimens with buckling-restrained dog-bone beam sections and one control specimen with a dog-bone beam section were tested under cyclic loading. The failure modes, hysteretic curves, skeleton curves, stiffness degradation ductilities, displacement ductility ratios, and energy dissipation capacities of the specimens were analyzed based on the experimental results to evaluate the seismic behavior of the proposed connections. The results indicated that the local buckling of the proposed connections was significantly reduced compared with the traditional connection with a dog-bone beam section under the condition of keeping the plastic hinges away from the beam–column connection core. The arrangement of the restrained plates in the dog-bone beam section had little effect on the bearing capacity and the initial stiffness, with errors all being within 6%. It is worth mentioning that the connection with restrained plates only on the flanges in the dog-bone beam sections showed a more obvious improvement in the deformation capacity and energy dissipation capacity of the connection, which increased by 21% and 16%, respectively. Additionally, high-quality welding between the beam and column, smooth cutting shapes on the weakened flanges, and the high-quality drilling of long slots at the fixed point in the restrained plates and the dog-bone beam sections should be guaranteed to improve the hysteretic stabilities of the proposed connections.

Keywords: steel moment connection; dog-bone beam section; buckling-restrained plate; pseudo-static test; seismic behavior

Citation: Feng, S.; Yang, Y.; Hao, N.; Chen, X.; Zhou, J. Experimental Study on Hysteretic Performance of Steel Moment Connection with Buckling-Restrained Dog-Bone Beam Sections. *Buildings* **2024**, *14*, 760. https://doi.org/10.3390/buildings14030760

Academic Editor: Binsheng (Ben) Zhang

Received: 13 December 2023
Revised: 9 March 2024
Accepted: 10 March 2024
Published: 12 March 2024

1. Introduction

Steel frame structures, as one of the most important modern building structures, are widely used worldwide due to the advantages of having light self-weight, excellent seismic performance, quick fast construction, flexible plane layout, and so on. However, it is noteworthy that numerous brittle fractures were observed to have occurred in or proximal to the welded joints connecting the beam bottom flange to the supporting column flange in steel moment-resisting frame systems during the 1994 Northridge earthquake in the United States and the 1995 Hyogoken-Nanbu earthquake in Japan [1–3]. A large number of buildings were demolished and rebuilt following the earthquake due to the aforementioned serious damage. The failure mode can be explained by Figure 1 [4] and the high-stress

concentration observed at the beam-to-column connection may interfere with the spread of the plastic area from the moment diagram along the beam of a steel moment-resisting frame when subjected to lateral seismic forces.

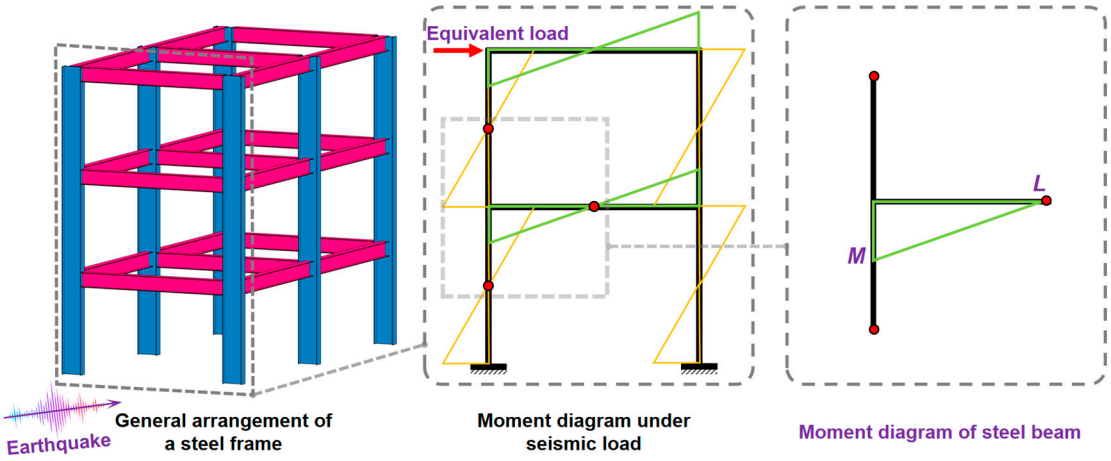

Figure 1. Moment state around the connection of a steel frame under earthquake loading.

To avoid the aforementioned brittle fractures occurring in or near the beam-to-column welded connection, numerous novel connections have been proposed to improve the seismic performance of steel moment-resisting frames in highly seismic regions. One of the proposed connections was a steel moment connection with a reduced beam section, which consisted of cuts made in the beam flanges or openings created in the beam webs near the core area of the beam-to-column connections [5–9]. It was conducive to the transfer of the larger resistant moment section from the beam-to-column connection to the beam span, so that the ductility failure mode of the proposed connection mode could be achieved. Among them, the transfer effect of weakening the flanges was better because the flexural strength primarily came from the flange plates. Therefore, steel moment connections with a dog-bone beam section have been extensively studied and applied in steel moment frames.

Plumier [5] first proposed the "dog-bone" idea, which meant the weakening of specific sections of structures for the deliberate establishment of reliable energy-dissipative zones during an earthquake event. This idea was tested and recognized for its contribution to ductility. A series of experimental studies about novel connections with a dog-bone beam section were conducted by Chen et al. [10–12]. The results indicated that the connection provided an enlarged plastic zone and alleviated strain levels in or near the weld between the beam end and column flange face compared to the traditional plastic hinge of a limited yielding area. As illustrated in Figure 2, they also presented the most intuitive explanation about the bending mechanism and comparison of plastic hinge positions between traditional beams and dog-bone beams. According to the geometric features of the weakened flanges, the cutting shapes can be divided into straight, variable, and radius. Moreover, different weakening parameters have a great influence on the seismic performance of the connections subjected to the same cutting shape [13–15]. Previous work has been conducted on different cut dog-bone shapes by Engelhardt et al. [16,17]. The results proved that the seismic performance of the dog-bone connection using the radius cut shape was superior to that of the dog-bone connection using the straight cut shape because stress concentration at the straight cut shape flanges led to early fracture. Based on an experimental study of eight dog-bone connections, Lee et al. [18] examined the impact of web connection types and panel zone strength on the cyclic behavior of the proposed connections. Their test results indicated that allowing the panel zone to deform inelastically at 0.01 rad reduced the magnitude of beam distortion by about half. Morshedi et al. [19] proposed a new type of connection with a double dog-bone beam section; the additional reduced section led to a wider plastic hinge. Moreover, this connection was optimized for the best seismic

performance by Gharebaghi et al. [20], and the optimum connection shapes revealed up to 39% better energy dissipation compared with the conventional dog-bone connection. Push-over tests, nonlinear static analyses, and time history analyses of steel moment-resisting frames with dog-bone beam sections were conducted by Huang et al. [21,22]. The plastic hinges on the beam first appeared at the dog-bone sections in the frames, and the performance advantage of the frames was verified. Some design suggestions and quantitative indices were proposed. Furthermore, based on previous research, the detailed design of a connection with a dog-bone beam section has been elaborated upon by different national standards [23–25].

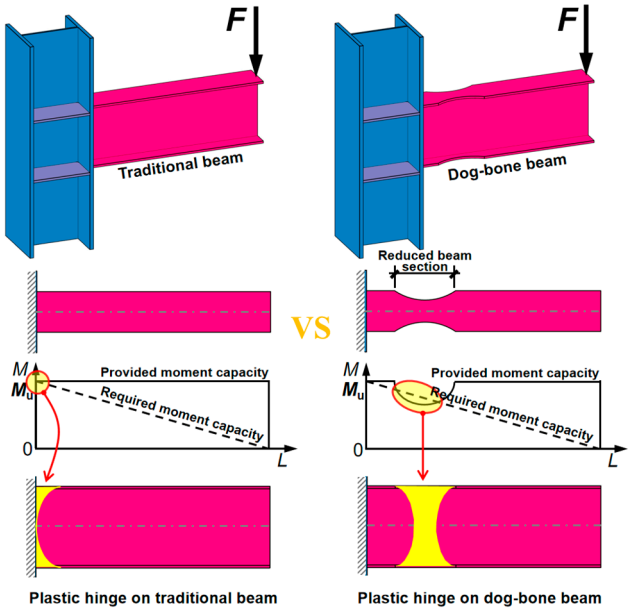

Figure 2. Comparison of plastic hinges between traditional beam and dog-bone beam.

Although the connection with the dog-bone beam section had good seismic performance, especially avoiding brittle fracture due to the transfer of plastic hinges, numerous pseudo-static tests revealed that the prevalent failure modes of the connections were local buckling of the web, local buckling of the flange, and lateral–torsional buckling of the beam [19,26,27]. These failure modes can seriously affect the performance of the connection. Therefore, the seismic performance of the connections will be further improved if some reasonable measures are applied to avoid these failure modes. Li et al. [28] proposed a construction measure for delayed local buckling by arranging stiffeners in the dog-bone beam section. Firstly, numerical experiments using a general finite-element method were conducted. Then, the seismic performance of the connection using the improvement measure was investigated by pseudo-static tests [29]. The research results indicated that strategically arranging stiffeners within the dog-bone beam section can effectively delay the onset of local buckling. Additionally, this arrangement contributed to increases in both the carrying capacity and plastic deformation capacity of the connections.

However, the dog-bone beam sections were very sensitive after arranging stiffeners, and the section with stiffeners could undergo brittle fracture in the welded parts under cyclic loading. In addition, a new dog-bone connection with double nut bolts and double shear tabs was proposed by Abar et al. [30]. The seismic performance of this connection was investigated analytically based on numerical analysis. The results showed that the proposed connection can efficiently delay the initiation of beam hinging, and the strength of the dog-bone section and energy dissipation were increased compared with the conventional dog-bone connection. Nevertheless, the seismic performance of this new connection has not yet been proven by experimental studies. In addition, Liu et al. [31,32] proposed a new buckling-restrained dog-bone connection composed of a buckling-restrained device

assembled outside the dog-bone beam section of the connections. An experimental study on a proposed connection and a common dog-bone connection was conducted to compare their hysteretic performance. The test results indicated that the hysteretic curve of the connection with the buckling-restrained device was more stable compared with the reference connection. Unfortunately, severe buckling at the beam flange end still occurred due to the binding between the buckling-restrained device and the dog-bone beam section being too tight.

Based on the aforementioned review, as shown in Figure 3, combined with the buckling-restrained mechanism [33,34], this paper presented a new steel moment connection with a buckling-restrained dog-bone beam section to address some of the above-mentioned shortcomings of typical dog-bone connections. It is worth noting that the low-elastic modulus material was sandwiched between the restrained plates and the dog-bone beam section. There are three types of proposed connections according to the different arrangements of restrained steel plates, including arranging the restrained plates only on the flanges, only on the web, and both on the flanges and webs of the dog-bone beam section. The major advantages of the proposed connections can be summarized as follows: (1) the obvious local buckling could be effectively reduced; (2) the dog-bone beam section could be more stabilized, in particular significantly weakening the global torsional instability; (3) under the premise of maintaining the bearing capacity and initial stiffness, its deformation capacity and energy dissipation could be significantly improved. The main reason is that the local buckling changes from a big single-wave buckling event to several small multi-wave buckling events under the constraint effect, which makes the plastic deformation of the dog-bone beam section more complete. The schematic diagram of the application scenario for the novel steel moment connection is shown in Figure 4. In order to facilitate structural construction, steel–concrete composite slabs could be employed as the floor slabs, which were composed of profiled steel sheets, studs, steel bars, and cast-in-place concrete. Among them, the studs were connected to the composite slabs and steel beam using fusion welding as shear connectors.

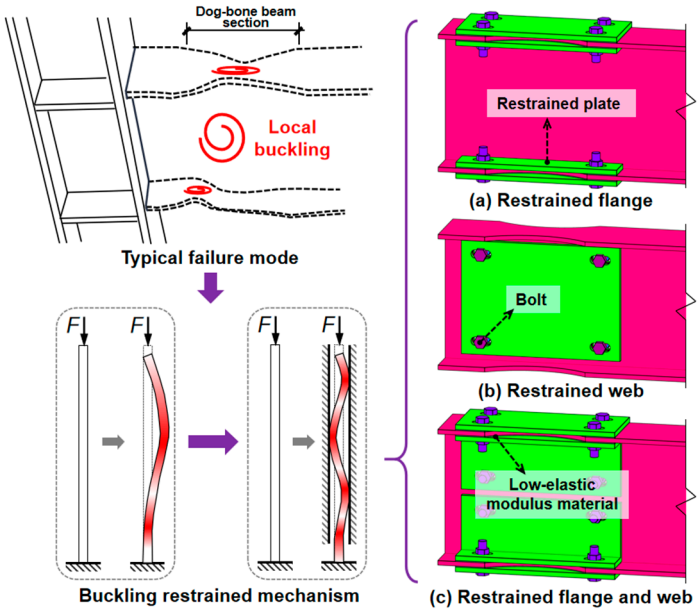

Figure 3. Steel moment connection with a buckling-restrained dog-bone beam section.

To explore the seismic behavior of the proposed connections, three connections with a buckling-restrained dog-bone beam section and one traditional connection with a dog-bone beam section were designed, fabricated, and tested under cyclic loading, with the main test parameter being the different restrained regions of the dog-bone beam section. Furthermore, the failure modes, hysteretic curves, skeleton curves, stiffness degradation,

displacement ductility ratios, and energy dissipation were thoroughly analyzed to verify the constraint of local buckling and the improvement in the seismic performance.

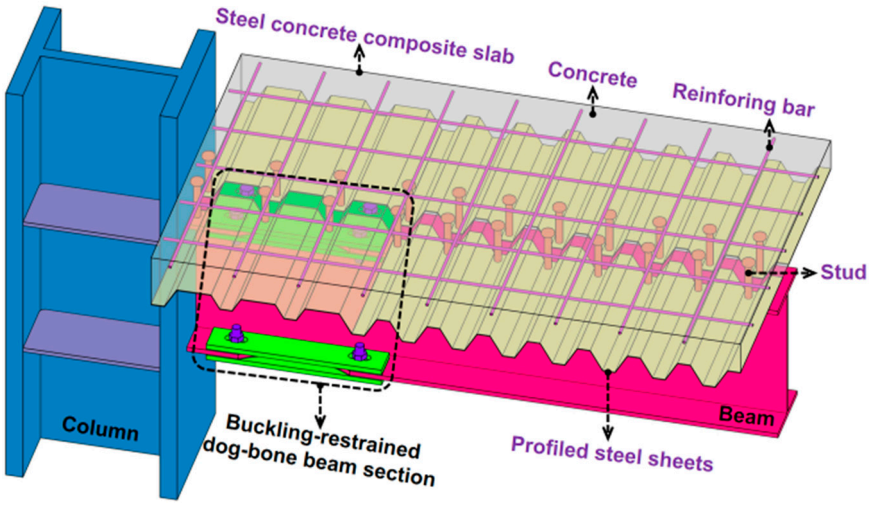

Figure 4. Schematic diagram of the application scenario for the novel steel moment connection.

2. Experimental Program

2.1. Specimen Design

Four specimens were designed in this experiment, including one control specimen (dog-bone beam section connection specimen) and three buckling-restrained dog-bone beam section specimens, as shown in Table 1. The last three specimens were wrapped with restrained steel plates in different parts of dog-bone beams, including the web, flange, and overall site of the web and flange. The steel beams in all the specimens were cut according to the standards [23,24], and the specific weakening details are shown in Table 1 and Figure 5.

Table 1. Parameter design of specimens.

ID	Sizes of Beam (mm)	Weakening Parameters			Restrained Region	Restrained Steel Plates
		a (mm)	*b* (mm)	*c* (mm)		
DC	HN350 × 175 × 7 × 11	120	260	40	-	-
DC-f					Flange	2~410 × 175 × 12, 4~410 × 71 × 12
DC-w					Web	2~410 × 294 × 12
DC-fw					Web and flange	2~410 × 175 × 12, 4~L152 × 81 × 12

Note: *a*, *b*, and *c* are fabrication detail parameters of the dog-bone beam section, as shown in Figure 5, and b_f and h_b are the beam flange width and depth, respectively; *m*, *x*, *y*, and *z* in '*m*~*x* × *y* × *z*' are the quantity, length, width, and thickness of the restrained steel plates, respectively.

The specimens' geometries are illustrated in Figure 5. H-shaped steel was welded vertically to the 40 mm thick end plate surface to form the steel beam, and the type of H-shaped steel was HN350 × 175 × 7 × 11, per Chinese standards, with a length of 1380 mm. It should be noted that there were no web access holes. In addition, all restrained plates were made of 12 mm thick steel plates after cutting and opening long slotted holes, and it was also necessary to open holes in the corresponding web and flange positions of the dog-bone beam section. Moreover, two 3 mm thick rubber slices were sandwiched between the dog-bone beam section and the restrained plates, and the dog-bone beam section, rubber slices, and the restrained plates were clamped via tightening high-strength friction bolts. It is worth noting that, in order to ensure that the dog-bone beam section could be fully deformed in the restrained plates, it was necessary to make the tightening torque of the two bolts in the same axis along the length of the steel beam different. Among

them, the bolts near the end plate were tightened with a big torque, and the initial torque was 250 N·m; and the other bolts were tightened with a small torque, and the initial torque was 50 N·m. In addition, the steel column was conducted by welding some stiffening ribs in a 1780 mm long steel shape whose type was H400 × 350 × 30 × 40.

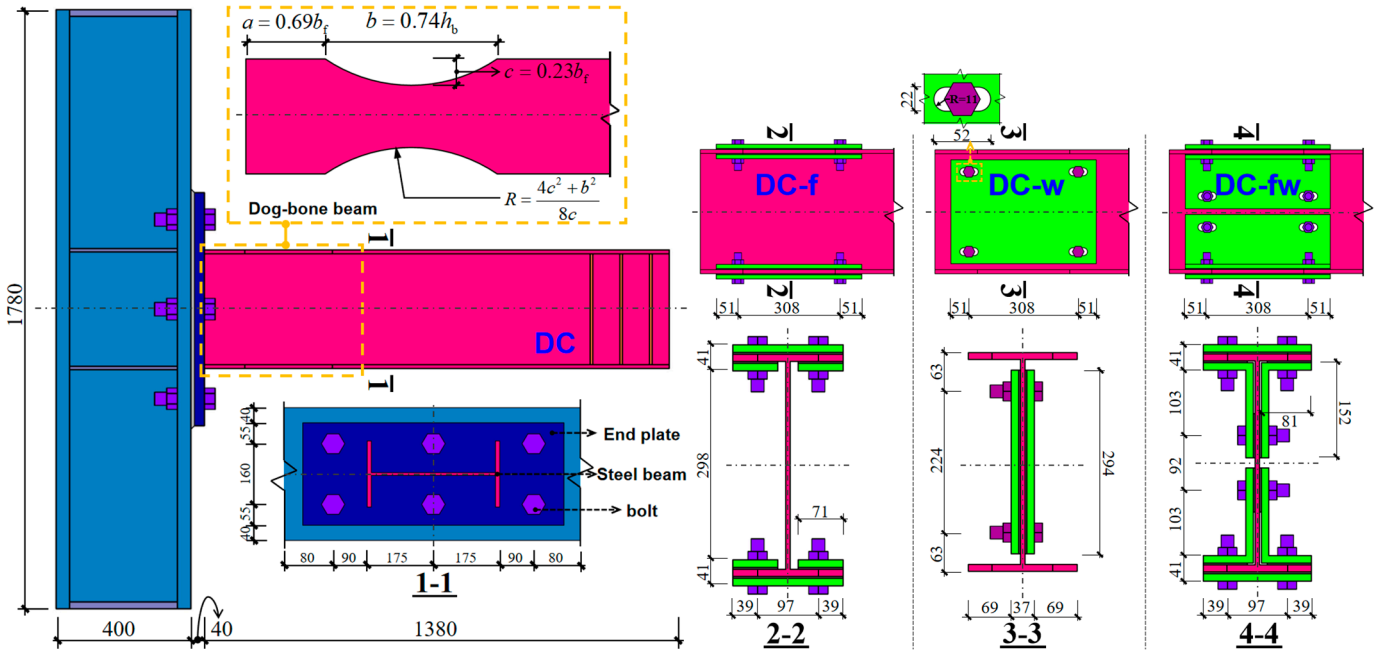

Figure 5. Design details of the specimens (unit: mm).

In general, the specimens were assembled by the aforementioned beam and column using high-strength bolted end plate connections. The diameter of the high-strength bolts was 36 mm, while their nominal tensile strength approximated 1000 MPa. In order to ensure a completely rigid connection, the connection was strengthened by welding between the end plate and the column face.

As shown in Figure 6, the assembly process of the proposed buckling-restrained dog-bone beam section can be divided into four major steps, taking specimen DC-f as an example for illustration: (1) drilling the long slots in the flange and web of the steel beam near the dog-bone beam section; (2) arranging the rubber slices on both sides of the plates of the dog-bone beam section to be restrained; (3) arranging the restrained plates on both sides of the rubber slices; (4) inserting the high-strength friction bolts into the holes, and tightening the bolts to connect the dog-bone beam section and restrained plates using a torque wrench.

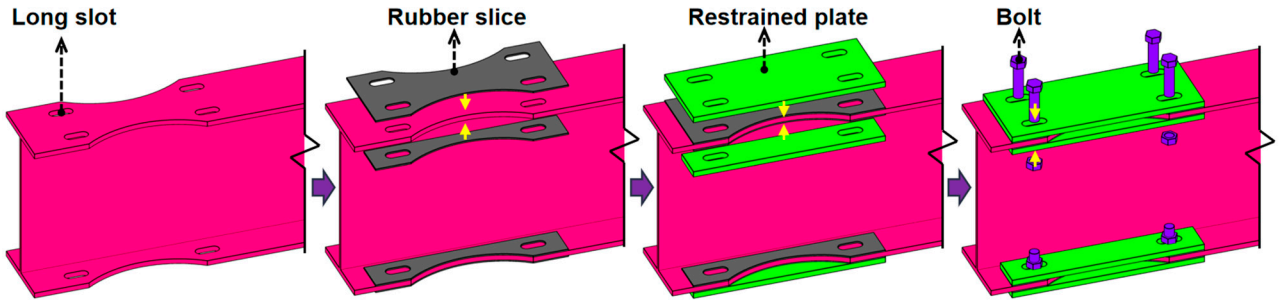

Figure 6. Assembling process of beam specimen DC-f.

2.2. Material Properties

The mechanical properties of the steel beam's web and flange, as well as the steel plate, are presented in Table 2. The pertinent tests were performed in accordance with the Chinese standard (GB/T 228.1-2010) [35].

Table 2. Mechanical properties of steel plates.

Sampling Locations	Steel Grade	Thickness T (mm)	Yield Strength F_y (MPa)	Tensile Strength F_u (MPa)	Young's Modulus E (MPa)
Web	Q235	7.0	334.8	457.3	2.05×10^5
Flange	Q235	11.0	271.7	434.7	2.05×10^5
Restrained steel plate	Q235	12.0	293.2	440.5	2.05×10^5

2.3. Test Setup and Cyclic Loading Protocol

The experimental procedure was carried out in the Key Lab of Structural Engineering and Earthquake Resistance at Xi'an University of Architecture and Technology. An overall view of the test set-up is shown in Figure 7. The test specimen was rotated 90 degrees for easy installation in the loading device. Reaction devices were arranged at both ends of the specimen column to restrain the slippage and rotation of the specimens during the testing process. Meanwhile, in order to avoid lateral–torsional buckling, the two lateral support arrangement was adopted to provide lateral restraints in the loading position. Polytetrafluoroethylene (PTFE) sheets were sandwiched between the lateral support and the loading device to reduce friction. An electrohydraulic servo actuator, with a maximum capacity of 1000 kN, was employed to apply lateral hysteretic load at the steel beam end.

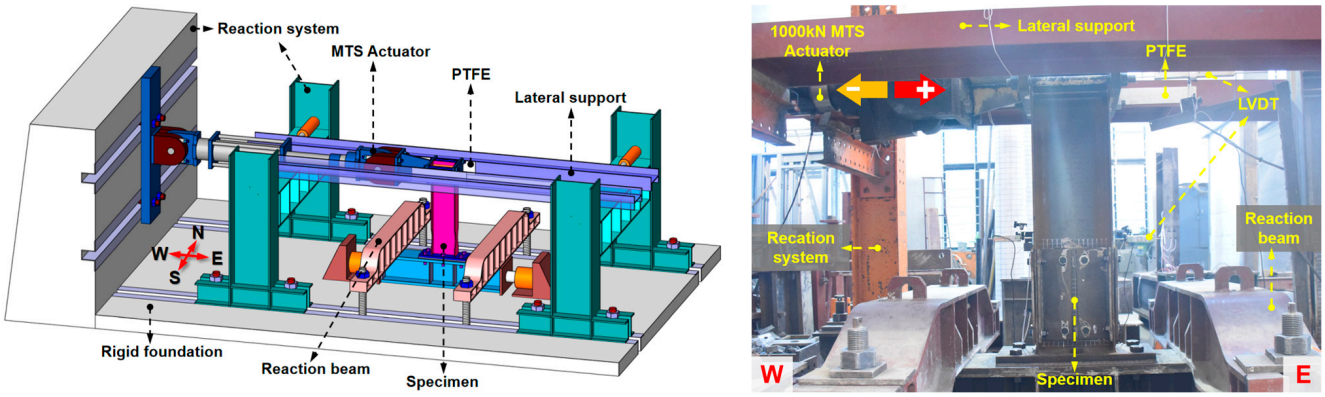

Figure 7. An overall view of the test set-up.

The test specimens were instrumented with a combination of linear variable differential transformers (LVDTs) and strain gauges to measure global and local responses (Figure 8). As shown in Figure 8, LVDT1 and LVDT2 were horizontally installed to measure the horizontal displacements of the beam end and the overall slip, respectively, during the testing process. LVDT3 and LVDT4 were also installed horizontally on the two side surfaces of the steel beam to measure the horizontal displacements of the dog-bone beam section. Moreover, the strains of the local webs and flanges in the applied steel beam were measured using strain foils. All the test data were recorded with a TDS602 data logger.

All the specimens were tested under reversed cyclic loading. The cyclic load was applied according to the displacement-control protocol, adhering to some suggestions from the Chinese code (JGJ/T 101-2015) [36]. The detailed loading procedure of the cyclic load is illustrated in Figure 9, where h represents the distance from the column center to the loading point of the beam end. Hence, the story drift ratio θ can be defined as the ratio of the loading displacement Δ to the distance h. Initially, five single cycles were applied with drift ratios of 0.10%, 0.15%, 0.45%, 0.65%, and 0.85%. Subsequently, cycles with drift

ratios of 1.00%, 1.35%, 1.70%, 2.05%, 2.40%, 2.75%, and 3.10% were applied, with each cycle being repeated three times. However, the actual loading protocol for specimen DC was incomplete, missing drift ratios of 0.65%, 2.05%, and 2.75%, owing to a negligent oversight by the experimental operators. The missing load values and energy dissipation values at these lacking load displacement levels for specimen DC could be estimated from the skeleton curve and energy dissipation curve, respectively. Furthermore, it is noteworthy that the experiments were terminated when the ultimate strength decreased by more than 15%.

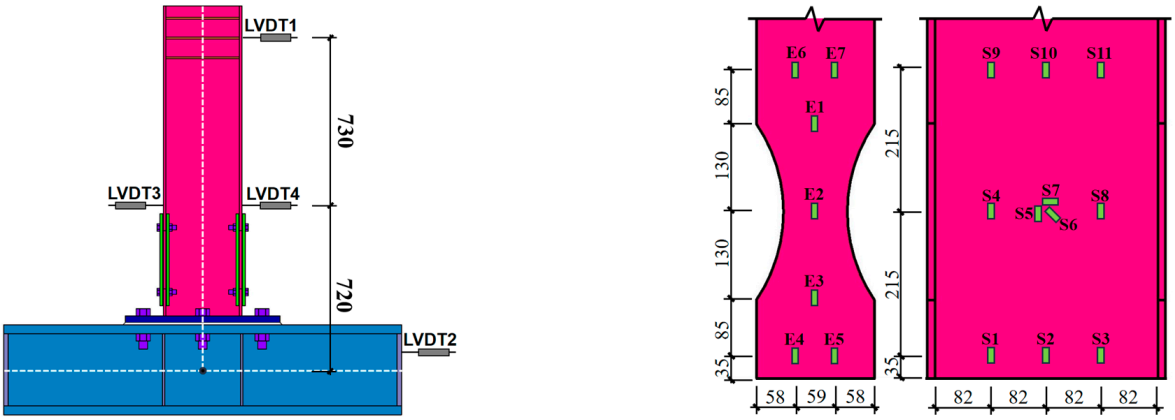

Figure 8. Layout of the LVDTs and the strain gauges (unit: mm).

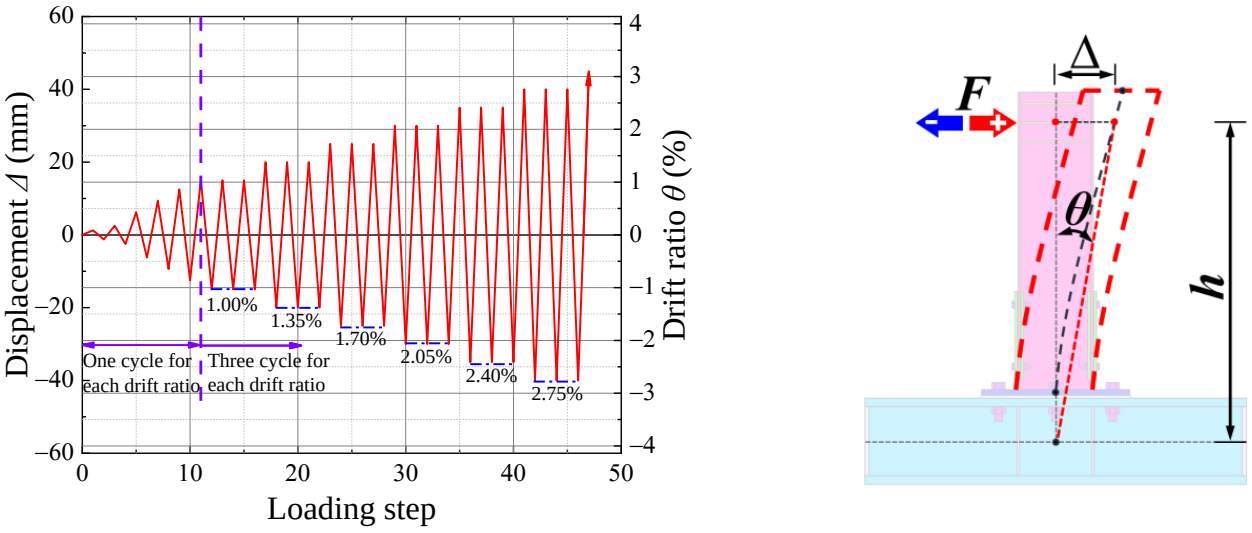

Figure 9. History of cyclic loading.

3. Test Results and Discussions

3.1. Test Observations

The testing phenomena of all the specimens are shown in Figure 10. As observed from Figure 10a, there were two different stages of deformation for specimen DC during the testing process. In the first stage, the specimen showed no obvious deformation when the drift ratio was smaller than 0.85%, indicating that the specimen remained in an elastic state at the beginning of the test. In the second stage, the dog-bone beam section of specimen DC experienced yielding and local buckling of the web and flange. Specimen DC failed due to obvious local buckling in the flange and web of the dog-bone beam section when the drift ratio reached 3.10%. Among them, the maximum out-of-plane deformations of the web and flange were 35 mm and 40 mm, respectively. However, the second-stage deformations of specimens DC-f, DC-w, and DC-fw were different from that of specimen DC. The restrained

specimens experienced yielding, local buckling, and fracture. For all but specimen DC-w, the target total story drift of 3.10% was reached.

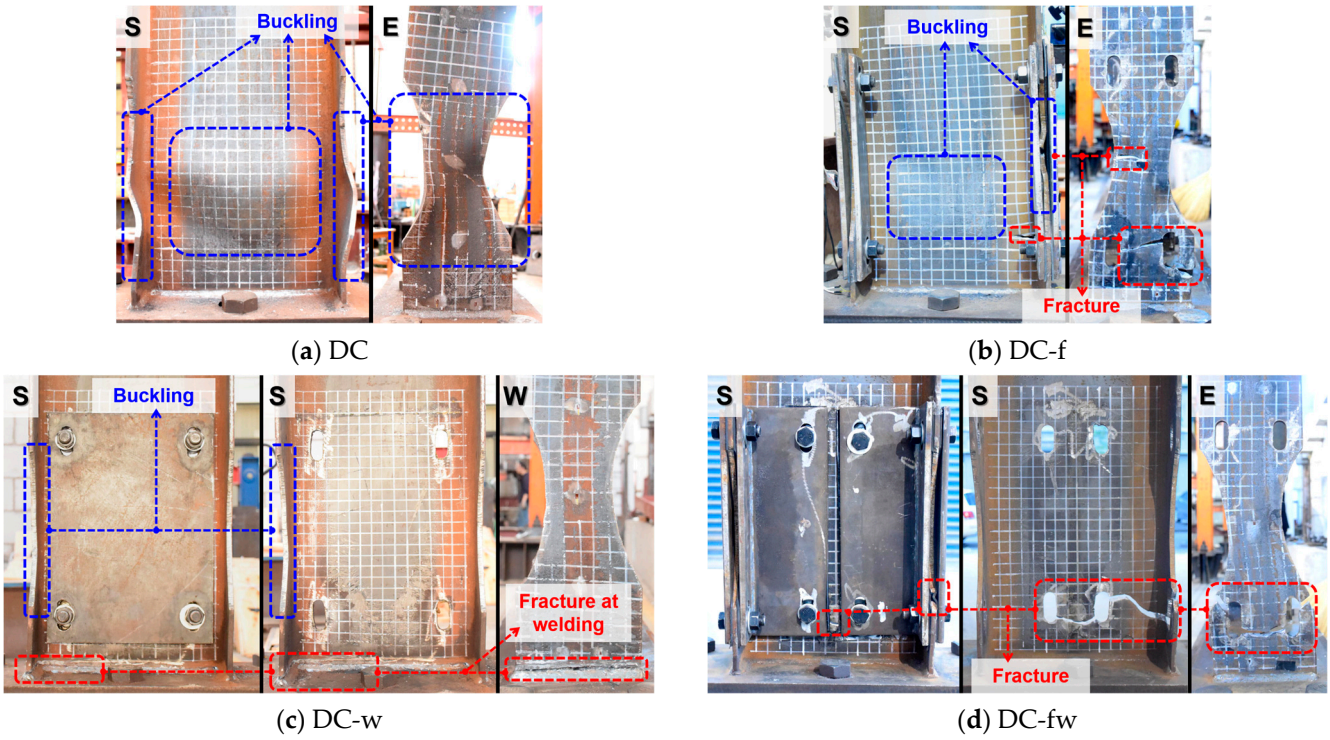

Figure 10. Failure modes of the specimens.

As observed from Figure 10, specimen DC-f failed due to obvious local buckling only in the web of the dog-bone beam section and successive local fracture in the minimum flange section and the flange section with long slots. The maximum out-of-plane deformation of the web of the dog-bone beam section was approximately 25 mm. Unfortunately, for specimen DC-w, the flange of the dog-bone beam section was buckling and the bottom flange unexpectedly fractured at the weld when the drift ratio reached 2.40%; then, the test stopped. In addition, specimen DC-fw failed due to the local fracture of the flange section with long slots near the end plate when the drift ratio reached 3.10%. The above fracture of the flange section was caused by the local stress concentration due to uneven cutting. In general, the damage of all the specimens occurred in the dog-bone beam section. It is worth mentioning that the obvious buckling of the restrained flange and web did not occur, and these results indicated that the restrained plates had a significant restraint effect.

The global deformation curves of all the specimens under 1.00%, 2.10%, and 3.10% drift ratios are illustrated in Figure 11. In Figure 11, H is the distance from the monitoring points of the beam to the column center. The displacement data at the height of 720 mm are the averages monitored by the LVDT3 and LVDT4. As shown in Figure 11, the displacement of specimen DC-f was 27.1% lower than that of specimen DC at the 720 mm height point when the loading drift ratio was 3.10%. This result indicated that limitations of the lateral displacement of the dog-bone beam section were most obvious by the arrangement of restraint plates on the flange of the dog-bone beam section.

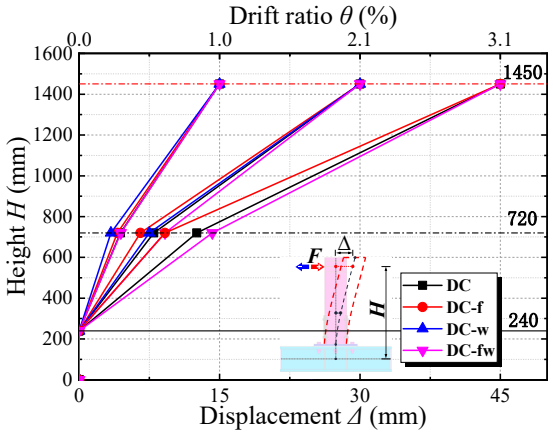

Figure 11. Global deformation curves of all the specimens under 1.00%, 2.10%, and 3.10% drift ratios.

3.2. Hysteretic Loops and Skeleton Curves

The hysteretic curves of all the specimens are depicted in Figure 12. As shown in Figure 12, the hysteretic curves of individual specimens were straight lines and almost without residual deformations when the drift ratio was smaller than 0.85%, indicating that the specimens were in the elastic state. The slope of the hysteretic curves decreased rapidly when the drift ratio was greater than 0.85%, and the curves of all the specimens tended to be full due to the residual deformation increasing with an increasing loading drift ratio. In addition, except for specimen DC-w, which was damaged earlier due to a welding quality problem, the other specimens exhibited stable hysteretic behaviors.

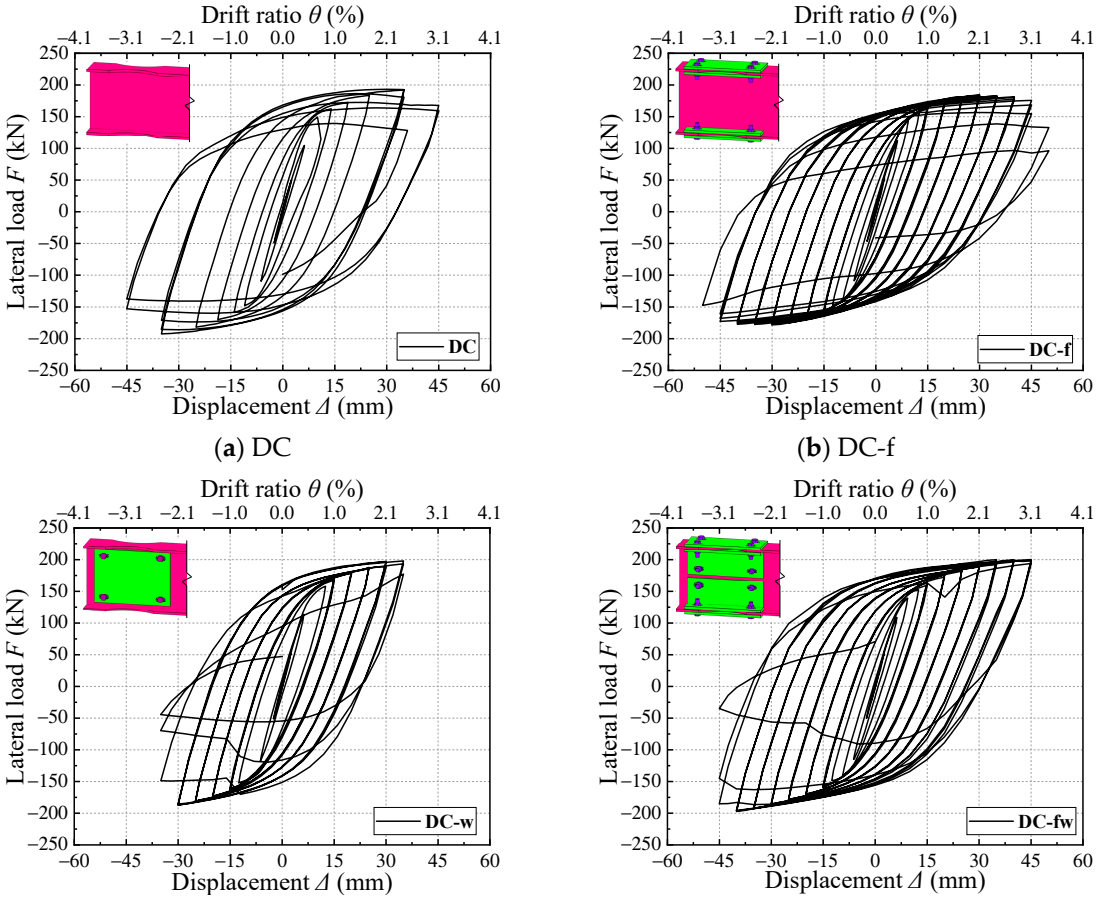

Figure 12. Hysteretic curves of the specimens.

The skeleton curves of the specimens are illustrated in Figure 13, and the peak loads of the specimens are summarized in Table 3. As observed from Figure 13, the skeleton curves of all the specimens experienced rapid load growths before the specimen yield, load stabilization, and slow load reduction as the loading displacement increased. In general, the skeleton curves were reflected in the shape of three fold lines, and there was little difference in the initial stiffness. In addition, the peak loads of specimens DC, DC-f, DC-w, and DC-fw were 192.26 kN, 181.23 kN, 192.48 kN, and 197.59 kN, respectively. Among them, the load-carrying capacities of specimens DC-w and DC-fw were 0.01% and 2.77% higher than that of specimen DC, and the load-carrying capacity of specimen DC-f was 5.74% lower than that of specimen DC. This result indicated that the restrained steel plates did not affect the bearing capacity of the specimen, although they limited the buckling of the dog-bone beam section.

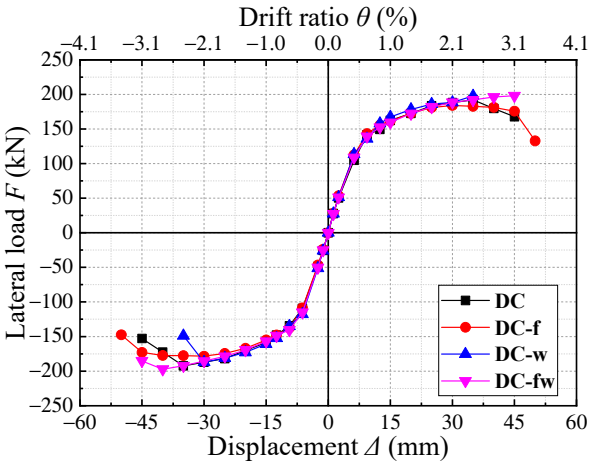

Figure 13. Skeleton curves of the specimens.

Table 3. Results of the displacement ductilities and energy dissipations of specimens.

Specimen ID	Direction	Δ_y (mm)	F_y (kN)	Δ_k (mm)	F_k (kN)	Average P_k (kN)	Δ_u (mm)	F_u (kN)	μ	Average μ
DC	Push	12.52	149.49	35.02	192.06	192.26	45.03	167.70	3.60	3.37
	Pull	13.54	152.54	35.01	192.45		42.41	163.58	3.13	
DC-f	Push	11.46	151.27	30.03	187.67	181.23	47.30	156.42	4.13	4.07
	Pull	12.27	146.94	30.07	178.44		49.25	151.68	4.01	
DC-w	Push	13.47	161.83	35.05	197.92	192.48	35.05	197.92	2.60	2.63
	Pull	12.71	152.82	30.04	187.04		33.71	158.92	2.64	
DC-wf	Push	13.21	154.50	45.03	197.98	197.59	45.03	197.98	3.41	3.35
	Pull	13.71	152.80	40.02	197.21		45.04	185.16	3.29	

Note: Δ_y, Δ_k, Δ_u, F_y, F_k, F_u, and μ are the yield displacement, peak displacement, ultimate displacement, yield load, peak load, ultimate load, and ductility ratio, respectively.

3.3. Stiffness Degradation

The effective stiffness was applied in this study to investigate the stiffness degradation behavior of the specimens [37], and it can be calculated using the following Equation (1):

$$K_{i+} = \frac{+P_i}{+\Delta_i} \text{ and } K_{i-} = \frac{-P_i}{-\Delta_i} \quad (1)$$

where K_{i+} and K_{i-} represent the effective stiffness values at the ith load displacement level during the positive half cycle and negative half cycle, respectively. Similarly, $+P_i$ and $-P_i$ denote the ultimate loads achieved at the ith load displacement level for the positive half cycle and negative half cycle, respectively. Lastly, $+\Delta_i$ and $-\Delta_i$ correspond to the respective load displacements.

The stiffness degradation curves of the test specimens are depicted in Figure 14. The lateral stiffnesses of all the specimens exhibited characteristic two-stage degradations, which included a rapid degradation of stiffness before reaching the 1.0% drift ratio, followed by a mild degradation after reaching the 1.0% drift ratio. The average initial stiffnesses of specimens DC, DC-f, DC-w, and DC-fw were 21.13 kN/mm, 20.66 kN/mm, 21.19 kN/mm, and 20.78 kN/mm, respectively. This result indicated that the initial stiffnesses of the restrained specimens had no obvious changes compared with that of the unrestrained specimen DC because of the low elastic modulus of the rubber slices sandwiched between the dog-bone beam section and the restrained plates. However, the stiffnesses of restrained specimens were obviously greater than that of specimen DC under the same loading displacement after reaching the drift ratio of 1.70%. This demonstrated that the buckling-restrained steel plate arrangements at the dog-bone beam section could reduce the stiffness degradation, so that the restrained specimens could maintain stable bearing capacities under large lateral deformation.

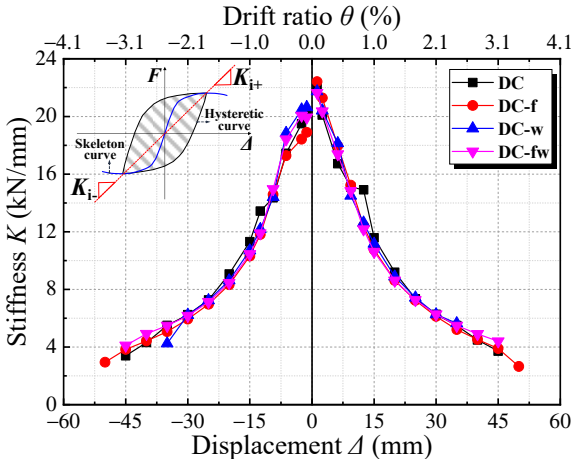

Figure 14. Stiffness degradations of specimens.

3.4. Displacement Ductility

The displacement ductility ratio μ can be determined as the ultimate displacement Δ_u divided by the yield displacement Δ_y. Figure 15 reveals the defining method of the yield displacement on the skeleton curve. As shown in Figure 15, Δ_u is the ultimate displacement at the ultimate point when the test load reached 85% of the peak load F_k, or the test was terminated, and the yielding displacement, Δ_y, is determined from the skeleton curve using the graphing method [37]. In Figure 15, the extension of the tangent to the ascending branch at the initial point of the skeleton curve is intersected by a horizontal line that passes through the peak load point at point A. Point B, located on the skeleton curve, is the projection of point A. Subsequently, the OB line is extended to intersect the horizontal line through the peak load point at point C. Finally, the projection of point C onto the skeleton curve can be regarded as the yield point.

According to the above method, the test results of the yield displacement, ultimate displacement, peak displacement, yield load, peak load, ultimate load, and the calculated displacement ductility ratios are listed in Table 3. As indicated in Table 3, the average displacement ductility ratios of specimens DC, DC-f, DC-w, and DC-fw were 3.37, 4.07, 2.63, and 3.35, respectively. This meant all the specimens exhibited acceptable levels of ductility except specimen DC-w. The ductility ratio of specimen DC-f improved by 20.77% compared with that of specimen DC, and this result indicated that the restrained steel plate arrangements at the flanges of the dog-bone beam section could effectively improve the deformation capacity and delay the rapid decline in the bearing capacity due to local buckling. In addition, the ductility ratios of specimens DC-w and DC-fw were 21.96% and 0.06% lower than that of specimen DC, respectively. This result indicated that the weld

quality problem could cause the hidden risk to the ductility of the beam–column joints. It is worth mentioning that there was no obvious effect on ductility by arranging restrained plates at both the web and flange of the dog-bone beam section. The main reason for this was that too many or too big holes in the section near the dog-bone beam section could significantly reduce the bearing capacity of the beam. Additionally, the perforation and cutting of the dog-bone beam area should have ensured that the cutting surface was as smooth as possible to avoid stress concentration under load.

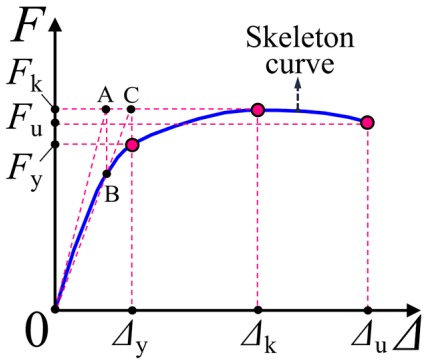

Figure 15. Defining method of the yield displacement on the skeleton curve.

3.5. Energy Dissipation Capacity

The cumulative energy dissipation was applied here to quantitatively analyze the energy dissipation capacity of each specimen. The energy dissipated during each loading cycle was represented by the area of the cyclic loops, and the cumulative energy dissipation could be acquired by the accumulation of the first circle area under each level of the loading displacement before the current circle. The cumulative energy dissipation curves of all the specimens are depicted in Figure 16, which show that the cumulative energy dissipation experienced slow load reduction before the specimen yield and rapid load growth as the loading displacement increased. As shown in Figure 16, the results of specimens DC, DC-f, DC-w, and DC-fw were 84.36 kN·m, 98.23 kN·m, 48.69 kN·m, and 87.70 kN·m, respectively. The cumulative energy dissipations of specimens DC-f and DC-fw were 16.44% and 3.96% greater than that of specimen DC. This result indicated that the energy dissipation capacities of the specimens were improved by the arrangement of the restrained steel plates at the dog-bone beam section, and the improvement in the specimen with only restrained flanges was the most obvious. In addition, the cumulative energy dissipation of specimen DC-f was 42.28% lower than that of specimen DC, and this was mainly caused by the weld fracture between the specimen beam and the end plate, leading to premature specimen failure.

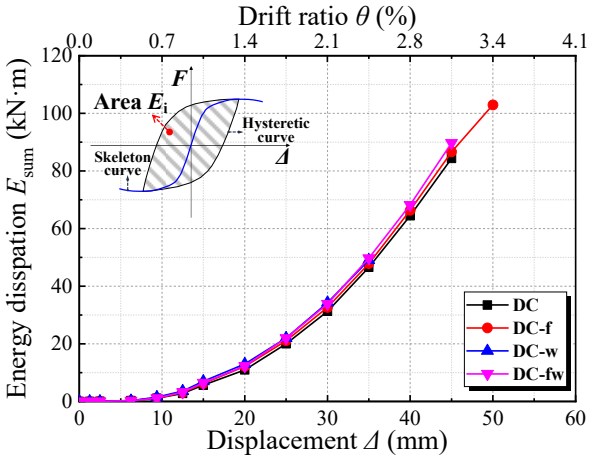

Figure 16. Cumulative dissipated energies of the specimens.

4. Conclusions

This paper proposed an innovative steel moment connection with a buckling-restrained dog-bone beam section, and the four specimens subjected to cyclic loading were examined to explore the hysteretic performance of the proposed connection. Based on the observations and discussion of the experimental results, a series of conclusions from this study can be summarized as follows:

- The initial yield area of all the specimens occurred in the dog-bone beam section during the testing process, indicating that the arrangement of the buckling-restrained steel plates did not affect the outward movement of the plastic hinge from the beam–column joint core area. According to the failure modes of the specimens, the arrangement of restrained steel plates could effectively restrain the local buckling of the dog-bone beam section and was conducive to the out-of-plane stability of the steel beam.
- The additional restrained steel plates in the dog-bone beam section had little influence on the bearing capacity and initial stiffness of the specimens, which were less than 6.00% and 3.00%, respectively. However, compared with the control specimen, the stiffness degradations of the restrained specimens were significantly reduced after the drift ratio of 1.70% was reached. Moreover, compared with the arrangement of restrained steel plates only on the web or both on the flange and web of the dog-bone beam section, the arrangement of restrained steel plates only on the flange caused a more obvious improvement in the deformation capacity and energy dissipation capacity of the connection, which were improved by 21% and 16%, respectively. This proved the validity of the proposed improvement method of the traditional steel moment connection with a dog-bone beam section in this paper.
- In order to give full play to the plastic deformation capacity of the dog-bone beam section, it was necessary to pay close attention to the construction quality of the proposed innovative steel moment connection. On the one hand, the welding quality of the steel beam and the end plate should be improved to prevent weld fractures [38]. On the other hand, the radius cutting and the long slot opening of the dog-bone beam section should be smooth to prevent stress concentration under loading [17]. In addition, the influence of the fixed point position and slot size on the hysteretic performance of the proposed connection should be further studied.
- The subsequent steps of the ongoing research encompass the following: (1) improving the connections in terms of the seismic performance and investigating the impact of different parameters on its seismic behavior, such as the weakening parameters of the dog-bone steel beam section, the thickness of the restrained plates, the size of the holes at the bolted connections in the restrained region, the tightening torque of the bolts, the restraint provided by the floor slab, the influence of vertical load, etc.; (2) establishing a theoretical model for the moment–rotation analysis of the proposed connections and proposing a seismic design method for the connections considering vertical loads based on the design abacus of Montuori [39]; (3) developing the numerical model of the connections; and (4) investigating moment-resisting frames and steel-braced frames using the connections on the seismic performance, with various parameters including the weakening parameters of the dog-bone beam section, the restraint effect of the restrained plates, the arrangement of braces, etc.

Author Contributions: Conceptualization, S.F. and Y.Y.; methodology, Y.Y.; software, S.F.; validation, S.F., Y.Y. and N.H.; formal analysis, N.H. and X.C.; investigation, X.C. and J.Z.; resources, S.F.; data curation, S.F.; writing—original draft preparation, S.F.; writing—review and editing, N.H. and X.C.; visualization, S.F.; supervision, Y.Y.; project administration, S.F.; funding acquisition, S.F. All authors have read and agreed to the published version of the manuscript.

Funding: This research was funded by the National Natural Science Foundation of China (Grant Nos. 52308202 and 52378190) and the Youth Innovation Team Research Project of the Education Department of Shaanxi Province (Grant No. 23JP080). The financial support is highly appreciated. In

addition, the authors of the paper are members of the Youth Innovation Team of Shaanxi Universities, Xi'an, China.

Data Availability Statement: The raw data supporting the conclusions of this article will be made available by the authors on request.

Conflicts of Interest: The authors declare no conflicts of interest.

References

1. Tremblay, R.; Timler, P.; Bruneau, M.; Filiatrault, A. Performance of steel structures during the 1994 Northridge earthquake. *Can. J. Civ. Eng.* **1995**, *22*, 338–360. [CrossRef]
2. Mahin, S.A. Lessons from damage to steel buildings during the Northridge earthquake. *Eng. Struct.* **1998**, *20*, 261–270. [CrossRef]
3. Nakashima, M.; Inoue, K.; Tada, M. Classification of damage to steel buildings observed in the 1995 Hyogoken-Nanbu earthquake. *Eng. Struct.* **1998**, *20*, 271–281. [CrossRef]
4. Chen, S.J.; Tsao, Y.C.; Chao, Y.C. Enhancement of ductility of existing seismic steel moment connections. *J. Struct. Eng.* **2001**, *127*, 538–545. [CrossRef]
5. Plumier, A. The dogbone: Back to the future. *Eng. J.* **1997**, *34*, 61–67.
6. Shin, M.; Kim, S.P.; Halterman, A.; Aschheim, M. Seismic toughness and failure mechanisms of reduced web-section beams: Phase 1 tests. *Eng. Struct.* **2017**, *141*, 198–216. [CrossRef]
7. Shin, M.; Kim, S.P.; Halterman, A.; Aschheim, M. Seismic toughness and failure mechanisms of reduced web-section beams: Phase 2 tests. *Eng. Struct.* **2017**, *141*, 607–623. [CrossRef]
8. Wang, X.; Yin, Z.; Li, Q.; Shen, S. Experimental study of beam-column connections with web opening in a low-rise steel frame. *Struct. Eng. Mech.* **2007**, *26*, 263–276. [CrossRef]
9. Tabar, A.M.; Alonso-Rodriguez, A.; Tsavdaridis, K.D. Building retrofit with reduced web (RWS) and beam (RBS) section limited-ductility connections. *J. Constr. Steel Res.* **2022**, *197*, 107459. [CrossRef]
10. Chen, S.J.; Yeh, C.H.; Chu, J.M. Ductile steel beam-to-column connections for seismic resistance. *J. Struct. Eng.* **1996**, *122*, 1292–1299. [CrossRef]
11. Chen, S.J.; Chu, J.M.; Chu, Z.L. Dynamic behaviour of steel frames with beam flanges shaved around connection. *J. Constr. Steel Res.* **1997**, *42*, 49–70. [CrossRef]
12. Chen, S.J.; Tu, C.T. Experimental study of jumbo size reduced beam section connections using high strength steel. *J. Struct. Eng.* **2004**, *130*, 582–587. [CrossRef]
13. Pachoumis, D.T.; Galoussis, E.G.; Kalfas, C.N.; Christitsas, A.D. Reduced beam section moment connections subjected to cyclic loading: Experimental analysis and FEM simulation. *Eng. Struct.* **2009**, *31*, 216–223. [CrossRef]
14. Pachoumis, D.T.; Galoussis, E.G.; Kalfas, C.N.; Efthimiou, I.Z. Cyclic performance of steel moment-resisting connections with reduced beam sections—Experimental analysis and finite element model simulation. *Eng. Struct.* **2010**, *32*, 2683–2692. [CrossRef]
15. Sofias, C.E.; Kalfas, C.N.; Pachoumis, D.T. Experimental and FEM analysis of reduced beam section moment endplate connections under cyclic loading. *Eng. Struct.* **2014**, *59*, 320–329. [CrossRef]
16. Engelhardt, M.D.; Winneberger, T.; Zekany, A.J.; Potyraj, T.J. The dogbone connection: Part II. *Mod. Steel Const.* **1996**, *36*, 46–55.
17. *FEMA-353*; Recommended Specifications and Quality Assurance Guidelines for Steel Moment Frame Construction for Seismic Applications. Federal Emergent Management Agency: Washington, DC, USA, 2000.
18. Lee, C.H.; Jeon, S.W.; Kim, J.H.; Uang, C.M. Effects of panel zone strength and beam web connection method on seismic performance of reduced beam section steel moment connections. *J. Struct. Eng.* **2005**, *131*, 1854–1865. [CrossRef]
19. Morshedi, M.A.; Dolatshahi, K.M.; Maleki, S. Double reduced beam section connection. *J. Constr. Steel Res.* **2017**, *138*, 283–297. [CrossRef]
20. Gharebaghi, S.A.; Tafreshi, R.F.; Fanaie, N.; Sarkhosh, O.S. Optimization of the double reduced beam section (DRBS) connection. *Int. J. Steel Struct.* **2021**, *21*, 1346–1369. [CrossRef]
21. Huang, B.; Shi, X. Research on seismic performance and seismic design of dog-bone connection light steel frames. *J. Wuhan Univ. Technol.* **2013**, *35*, 112–115. (In Chinese)
22. Shen, J.; Kitjasateanphun, T.; Srivanich, W. Seismic performance of steel moment frames with reduced beam sections. *Eng. Struct.* **2000**, *22*, 968–983. [CrossRef]
23. *FEMA-350*; Recommended Seismic Design Criteria for New Steel Moment-Frame Buildings. Federal Emergent Management Agency: Washington, DC, USA, 2000.
24. *GB 50017-2017*; Standard for Design of Steel Structures. China Architecture and Building Press: Beijing, China, 2017. (In Chinese)
25. *BS EN 1998-3*; Eurocode 8—Design of Structures for Earthquake Resistance—Part 3: Assessment and Retrofitting of Buildings. European Committee for Standardization: Brussels, Belgium, 2005.
26. Nakashima, M.; Kanao, I.; Liu, D. Lateral instability and lateral bracing of steel beams subjected to cyclic loading. *J. Struct. Eng.* **2002**, *128*, 1308–1316. [CrossRef]
27. Wang, Y. Development of the research on new type ductile connection in steel moment resisting frames. *J. Qingdao Technol. Univ.* **2006**, *27*, 1–6. (In Chinese)

28. Li, J.; Yu, Z.; Li, F. Experimental study on performance of dog-bone moment connections considering local buckling. *Prog. Steel Build. Struct.* **2013**, *15*, 6–10. (In Chinese)
29. Li, F.X.; Kanao, I.; Li, J.; Morisako, K. Local buckling of RBS beams subjected to cyclic loading. *J. Struct. Eng.* **2010**, *135*, 1491–1498. [CrossRef]
30. Abar, B.M.; Bakhshayesh, Y.; Garcia, R.; Hajirasouliha, I. A new energy-dissipating RBS connection with double-nut-bolts: Seismic performance assessment and design methodology. *Eng. Struct.* **2023**, *293*, 116596. [CrossRef]
31. Liu, C.; Wu, J.; Xie, L. Seismic performance of buckling-restrained reduced beam section connection for steel frames. *J. Constr. Steel Res.* **2021**, *181*, 106622. [CrossRef]
32. Liu, C. Hysteretic Behaviour Research of Buckling-Restrained Reduced Beam Section Connections for Steel Frame. Master's Thesis, Southeast University, Nanjing, China, 2019. (In Chinese).
33. Fujimoto, M.; Wada, A.; Saeki, E. A study on the unbonded braces encased in buckling-restraining concrete and steel tube. *J. Struct. Eng.* **1988**, *114*, 249–258.
34. Yan, H.; Pan, P.; Wang, Y.; Makino, T.; Qi, X. Experimental study of buckling-restrained braces with in-line steel core plate encased in double web wide flange steel outer unit. *J. Build. Struct.* **2012**, *33*, 142–149. (In Chinese)
35. *GB/T 228.1-2010*; Metallic Materials-Tensile Testing—Part 1 Method of Test at Room Temperature. Standards Press of China: Beijing, China, 2010. (In Chinese)
36. *JGJ/T 101-2015*; Specification for Seismic Test of Buildings. China Architecture and Building Press: Beijing, China, 2015. (In Chinese)
37. Yang, Y.; Feng, S.; Xue, Y.; Yu, Y. Experimental investigation on the seismic behaviour of innovative self-centring precast steel-concrete hybrid frames. *Eng. Struct.* **2021**, *239*, 112222. [CrossRef]
38. Jones, S.L.; Fry, G.T.; Engelhardt, M.D. Experimental evaluation of cyclically loaded reduced beam section moment connections. *J. Struct. Eng.* **2002**, *128*, 441–451. [CrossRef]
39. Montuori, R. The influence of gravity loads on the seismic design of RBS connections. *Open Constr. Build. Technol. J.* **2014**, *8*, 248–261. [CrossRef]